LANGMUIR

pubs.acs.org/Langmuir Article

Drop Adhesion Force as a Measure of the Solid−Liquid Area Fraction on Cassie−Baxter Superhydrophobic Surfaces

Petr Druzhinin,[¶] Iana Fomicheva,[¶] George Sarau, Anca Mazare, Bihai Song, Wolfgang H. Goldmann, Silke H. Christiansen, and Alexander B. Tesler*

Cite This: *Langmuir* 2026, 42, 8269−8279 Read Online

ACCESS | Metrics & More | Article Recommendations | Supporting Information

ABSTRACT: Superhydrophobic surfaces have attracted considerable attention due to their remarkable ability to repel aqueous media by trapping an air layer. However, estimating the solid−liquid area fraction is challenging due to the complexity of their intrinsic properties and the limited resolution of methods for assessing contact area. We demonstrated that solid−liquid area fraction can be measured using reflectance optical microscopy, which provides a millimeter field of view with a micrometer lateral resolution. However, this method depends on the surface's optical characteristics. To simplify these measurements, this study examines the drop adhesive force as a means of quantifying solid−liquid area fraction. Utilizing a controlled experimental setup, we investigated the relationship between drop adhesive forces and solid−liquid area fraction. After considering various surface geometries obtained by laser and electrochemical treatments, we engineered 23 surfaces with solid−liquid area fractions ranging from 0.1% to ∼50%. Our results show that the adhesive force exerted by droplets on these surfaces increases linearly with the degree of air entrapment beneath the liquid. This provides a measurable indicator of their Cassie−Baxter superhydrophobicity. This research advances our fundamental understanding of plastron on superhydrophobic surfaces, facilitating the development of highly repellent, ultraslippery surfaces.

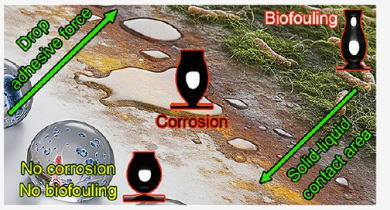

INTRODUCTION

Wetting is defined as the interaction between a liquid and a solid surface.[1] It is a complex phenomenon that poses significant challenges and complexities across a broad range of biological, ecological, and engineering processes.[2] Regulating the wetting properties of surfaces is fundamental and has profound implications for results in efficiency, safety, cost-effectiveness, and performance in a variety of industries. Wetting is characterized by two specific apparent contact angles (CAs), which are the macroscopically measurable angles between the droplet and the solid at the three-phase contact line.[3] The CAs can be calculated using the Laplace−Young equation at the droplet edge and the baseline, which is the line connecting the two three-phase contact points in a side-view image of a droplet.[4] These two specific angles represent the advancing and receding metastable CAs on a given surface. The difference between them is known as contact angle hysteresis (CAH).[5] In practice, wetting is described relative to the surface's hydrophilicity or hydrophobicity. The surface is considered hydrophilic if the water contact angle is less than 90°. If the water CA is smaller than 10°, the surface is termed superhydrophilic. A surface with a water CA greater than 90° is considered hydrophobic, and when the water CA exceeds 150°, it is termed superhydrophobic.

Low-wettable surfaces, such as superhydrophobic surfaces (SHS), have significant potential in various scientific and technological domains.[6,7] However, current advances in this field have yet to align with industry requirements.[8,9] A key challenge is implementing CA measurements, which are known to present certain difficulties.[10] From an experimental perspective, measuring these values for surfaces with CA higher than >170°, and CAH lower than <1° is challenging. The former is difficult because minor changes in the baseline location result in unreliable CAs,[11] while the latter is due to the high mobility of drops and their tendency to rapidly roll off from these surfaces. Additionally, the Laplace−Young equation provides a satisfactory fit to the axisymmetric drop shape. However, deviations from symmetry, such as asymmetry or elongation resulting from gravity or substrate interactions, can lead to substantial inaccuracies in fitting CA values.[12] From a conceptual perspective, conventional goniometric measurements do not explicitly reveal the characteristics of the plastron (*e.g.*, a trapped air layer) or the stability of the wetting state of solid surfaces. Due to variability in surface texture and/or chemistry, multiple wetting regimes may exist on the same surface. These include the Cassie−Baxter or Wenzel states, some of which are stable and others are metastable.[13]

Not all superhydrophobic surfaces are resistant to wetting and wetting-related phenomena, but those with plastron that

Received: November 9, 2025
Revised: February 1, 2026
Accepted: February 5, 2026
Published: February 12, 2026

https://doi.org/10.1021/acs.langmuir.5c05888
Langmuir 2026, 42, 8269−8279

effectively separates a liquid from direct contact with the solid surface. We recently demonstrated that superhydrophobic aluminum substrates with comparable CA and hysteresis values exhibited a seven-order-of-magnitude difference in their corrosion current density.[14] Furthermore, when immersed in artificial seawater, one set of samples substantially corroded within the first 12 h, while the second set remained undamaged after 415 days of continuous immersion. This significant variation in corrosion resistance can be attributed solely to plastron properties and their stability over time. However, there is currently no standardized method for characterizing the plastron of superhydrophobic surfaces. Previous attempts to measure plastron at the microscopic scale (*e.g.*, confocal microscopy) have not provided sufficient lateral information,[15,16] while measurements at the macroscopic scale (*e.g.*, still digital imaging[17,18]) have not been sensitive enough.[14] Recently, we proposed using optical reflectance microscopy to measure plastron on a macroscopic scale with microscopic resolution.[3,19] However, as we demonstrated, plastron shape, size, and surface coverage can differ substantially on various samples.[3,14,19,20] Given the challenges associated with measuring hierarchical surface roughness, CAs, and CAH, the wetting community requires a straightforward, rapid, and efficient approach to assess and characterize extremely low-wettable surfaces.

In recent years, research on wetting low-wettable surfaces has focused on measuring and understanding dynamic adhesion forces.[21−25] Several techniques have been developed to characterize adhesive forces on superhydrophobic surfaces, offering enhanced sensitivity compared to conventional goniometric methods.[10,26−32] These techniques can be categorized into two approaches: one that measures vertical adhesion (*i.e.*, the force acting vertically on the contact surface) and one that measures lateral adhesion (*i.e.*, friction) when the drop moves along the contact plane.[26] However, to the best of our knowledge, these techniques have not been used to correlate plastron developed on superhydrophobic surfaces with drop adhesive forces due to the challenges associated with plastron measurements.

In this study, we explore the correlation between drop adhesive forces[33] and the solid−liquid area fraction of superhydrophobic surfaces. Solid−liquid area fraction is defined as the portion of a surface that is in direct contact with liquid compared to plastron. To achieve a particular solid−liquid area fraction, we modified the metallic surfaces of the Ti6Al4V alloy by laser irradiation. This process formed stripes, squares, or inverted pyramids on a scale of tens of microns, with various peak-to-valley area ratios. Then, electrochemical anodization was applied to create hierarchical morphology. These treatments enabled the solid−liquid area fraction to vary from 0.1% to around 50%. Notably, even at the highest solid−liquid area fraction values, drops larger than 10 μL are completely retracted from the substrates (see Movies S1 and S2). Note that a 10 μL drop on a superhydrophobic surface already introduces significant measurement errors due to gravity, which distorts the shape of the drop, causing it to deviate from a perfect sphere.[12,34] As a result, the CA measurements were impractical. Our findings suggest that drop adhesive force increases linearly with the solid−liquid area fraction. Consequently, analyzing drop adhesive force is a quick way to assess the existence and coverage fraction of plastron. This approach enables us to identify the most promising ultraslippery candidates for further evaluation in wetting-repellent applications. This can be done even before measuring more complex surfaces and wetting parameters, such as surface roughness, the most stable CA, CAH, and solid−liquid area fraction.

MATERIALS AND METHODS

Materials

Titanium alloy (Ti6Al4V) plates were purchased from SELFAN Fine + Metal GmbH (Germany) and cut to dimensions of 40 × 50 × 0.8 mm. The following products were purchased from Carl Roth (Germany): hydrogen peroxide, acetone, and ethanol. The phosphate ester of the mixed length of fluorinated alkyl chains surfactant ($(CF_3-(CF_2)_{5-9}-(CH_2)_2-O)_2-POOH$, hereafter abbreviated as FS) was purchased from Chemguard, USA. All experiments were carried out using deionized (DI) water (18.2 MΩ · cm, ELGA, Purelab Ultra, U.K.).

Laser-Treated Surfaces

The as-produced Ti alloy plates were irradiated using a linearly polarized picosecond laser (Cepheus, Photon Energy GmbH, A Hitachi Group Company) with a wavelength of 1,064 nm and a pulse duration of 12 ps. The output laser scanning strategy on the target surface was controlled by a two-dimensional scanning galvanometer system (SCANcube from Scanlab, Germany), which was mounted on a one-coordinate Z translator. The *F*-theta objective lens (f = 100 mm) was utilized to focus the laser onto the surface of the Ti alloy plates mounted on a computer-controlled *XY* two-axis translation stage. The focused diameter of the Gaussian-profile laser beam after the lens was approximately 32 μm at $1/e^2$ of its maximum intensity. The laser processing experiments were conducted in an ambient atmosphere at the normal incidence of the laser beam.

Electrochemical Anodization Treatment

Prior to anodization, the substrates were thoroughly cleaned using ultrasonication in acetone and ethanol for a duration of 10 min to ensure removal of any contaminants. The electrochemical cell consists of a stainless steel (316 grade) counter electrode of comparable size to a Ti alloy sheet. A Ti alloy sheet was used as a working electrode, and a 1.5 M NaOH aqueous solution as electrolyte. In total, 1 vol % of H_2O_2 was added to the NaOH electrolyte just before anodization. The counter and working electrodes were placed 20 mm apart. Anodization was carried out at an applied potential of 15 V for 30 min. The anodized samples were then removed from the electrolyte, rinsed with DI water, and dried under a stream of air.

Low-Surface-Energy Coating

The FS surfactant, characterized by a surface tension of $\gamma = 15.3 \pm 0.3$ mN m^{-1} (10 g), was meticulously dissolved in 1 L of 95:5 vol % ethanol:H_2O using ultrasonication. The solution was stored in a closed container under ambient conditions. Either bare laser-treated or laser-treated and anodized samples were immersed in the surface modifier solution, and a plastic cover to prevent ethanol evaporation was used to seal the surfactant container. The container containing the high surface roughness samples was placed in a preheated muffle furnace set at +60 °C for a duration of 30 min. The low surface-energy metallic substrates were then removed from the surface modifier solution, rinsed with ethanol, and dried under a stream of air.

Drop Adhesive Force Measurements

In an r - θ type liquid bridge system, the meridian interface contour is governed by the general Young−Laplace equation, which accounts for the balance between gravitational, interfacial, and adhesion forces.[22,35] By fitting experimental coordinate data $\{x_i, z_i\}$ to the equation, physical parameters such as the contact angle θ, contact radius r, and capillary pressure ΔP can be determined with high precision. These values are then used to calculate the tensile adhesion force, or Drop Adhesion Force (DAF), denoted as f_t. DAF results from the force balance between interfacial tension (F_γ) and capillary pressure ($F_{\Delta P}$) and is defined as follows

https://doi.org/10.1021/acs.langmuir.5c05888
Langmuir 2026, 42, 8269−8279

$$f_t = F_\gamma - F_{\Delta P} = \gamma \cdot 2\pi r \cdot \sin\theta - \Delta P_{z=0} \cdot \pi r^2 \quad (1)$$

where f_t is the drop adhesion force, γ is the interfacial tension, and $2r$ is the contact diameter. $\Delta P_{z=0}$ is the capillary pressure difference at given $z = 0$, *i.e.*, at the solid surface. Depending on whether the liquid bridge exerts a pulling or pushing force on the solid surface, the DAF value can be positive or negative. To standardize this force across different bridge sizes and geometries, it is normalized to the contact circumference, yielding the "drop adhesion force *per* unit length, f_u

$$f_u = \frac{f_t}{2\pi r} \quad (2)$$

See the corresponding section in the Supporting Information for more details.

The LSA 60 surface analyzer (Lauda Scientific, Germany), equipped with a lifting stage, was used to measure the drop adhesive force. A 30 μL drop was dispersed on the needle with a diameter of 1.8 mm. The automatic stage with the sample was moved up to approach the sample surface with the drop. The stage was then advanced at a rate of 0.016 mm s^{-1} to a distance of 1 mm, which resulted in force drop compression. This position was maintained for 1 s to achieve maximum compression. The stage was then retracted at a rate of 0.016 mm per second until the drop was completely detached from the surface. At least three independent measurements were performed on each surface treatment. The process was video recorded by a CCD camera at a rate of 1 frame *per* second. The drop shape was then calculated using the Laplace–Young fit with SurfaceMeter software provided by the manufacturer to acquire the drop adhesive force.[21,36,37]

Solid–Liquid Area Fraction Measurements

A 10 cm-diameter polystyrene Petri dish was filled with DI water to a height of ∼1 cm. The low-energy samples were then immersed underwater, forcing them to sink to the bottom. The solid–liquid area fraction was obtained using a Zeiss Axio Imager 2 light microscope using an ×5 objective in bright-field reflectance mode (see Scheme 1). This fraction was analyzed using the MIPAR image analysis software (version 4.5.0) using the obtained optical reflectance microscopy images. To determine the boundaries of the solid–liquid area fraction and its subsequent segmentation, the adaptive threshold script was used. This script facilitates selecting pixels based on their intensity relative to the statistics of the surrounding neighborhood. Pixel values are then compared to their local average gray scale value, which ranges from 0 to 255. After comparing the software-separated solid–liquid fractions for several images at different pixel-to-local mean value threshold ratios, a ratio of 0.92 was chosen as optimal because it most accurately represents the boundary between the solid and liquid fractions. Since the optical images were acquired under the same illumination and exposure conditions, the threshold ratio of the pixel value to the local mean value remained constant. Consequently, if a pixel value is less than 92% of the average gray scale value in a window centered around it, the pixel will be selected as part of the solid–liquid area fraction. Window sizes were selected according to the size of the structures created (*e.g.*, strips or squares). A minimum of three independent measurements were performed for each surface treatment to ensure statistical analysis.

Physicochemical Characterization

We investigated the surface morphology using field-emission scanning electron microscopy (FE-SEM, Zeiss Crossbeam 550), which was equipped with energy-dispersive X-ray spectrometry (EDX, Oxford Instruments, U.K.). The chemical composition of the samples, both with and without the FS coating, was evaluated using X-ray photoelectron spectroscopy (XPS, PHI 5600, USA). The samples were mounted on the sample holder and introduced into the ultrahigh vacuum chamber. Survey and high-resolution scans were performed to obtain detailed spectra of the core-level electrons for C 1s, O 1s, Ti 2p, N 1s, V 2p, F 1s, and P 2p. Note that the spectra were calibrated with the C 1s peak at 284.8 eV, and the peak fitting was performed in the Multipak software (version 9.9.0.19). The roughness of the laser-ablated Ti alloy samples was measured using a DCM3D confocal laser microscope (Leica Inc., Germany), which combines confocal and interferometry technologies. Measurements were taken with the ×20 objective. The 201 slices were measured with a step size of 0.2 μm. The topography images were then characterized using Gwyddion 2.65 software to calculate the mean area roughness (S_a) and the dimensionless Wenzel roughness parameter (r_W) over a 0.64 × 0.48 mm^2 area. Attenuated total reflectance Fourier transform infrared spectroscopy (ATR-FTIR) was performed using an Agilent Cary 600 FTIR spectrometer. FTIR spectra were recorded between 1500–700 cm^{-1} with 16 scans and at a resolution of 4 cm^{-1}. The free IR beam in air was measured after the sample and used as a background. We used the quantum cascade laser micro-IR spectrometer Spero-QT 340 and ChemVision software (version 3.4.0, Daylight Solutions, USA) for IR imaging. The instrument covers a spectral range of 1,900 to 958 cm^{-1} with a spectral resolution of 2 cm^{-1} using the ×4 objective (0.3 NA) and produces an image with a pixel size of 4.25 μm × 4.25 μm.

Scheme 1. Schematic Representation Illustrates the Solid-Liquid Area Fraction Measurement Experiment

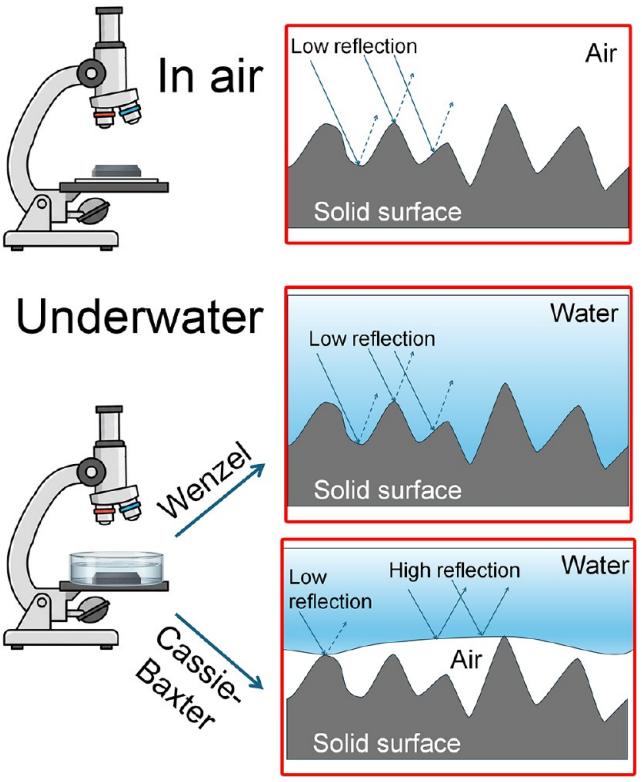

RESULTS AND DISCUSSION

Physicochemical Characterization of Laser-Treated Ti Alloy Surfaces

Figure 1a–k shows scanning electron microscopy (SEM) images of laser-treated titanium alloy surfaces and their corresponding cross-sectional topographies. Figure S1 indicates higher-magnification SEM images. Figures 1l_1 and S1l display typical images of the as-manufactured Ti-6Al-4V alloy surface for comparison. The mean surface roughness (S_a) of the as-manufactured Ti substrates was 1.0 μm, as determined by a confocal laser microscope. In addition to S_a, we provide the dimensionless Wenzel roughness parameter, which is used in theoretical calculations of plastron and Cassie–Baxter wetting state stability.[13,38] Thus, it must be determined for any superhydrophobic surface to allow for further comparison.

https://doi.org/10.1021/acs.langmuir.5c05888
Langmuir 2026, 42, 8269–8279

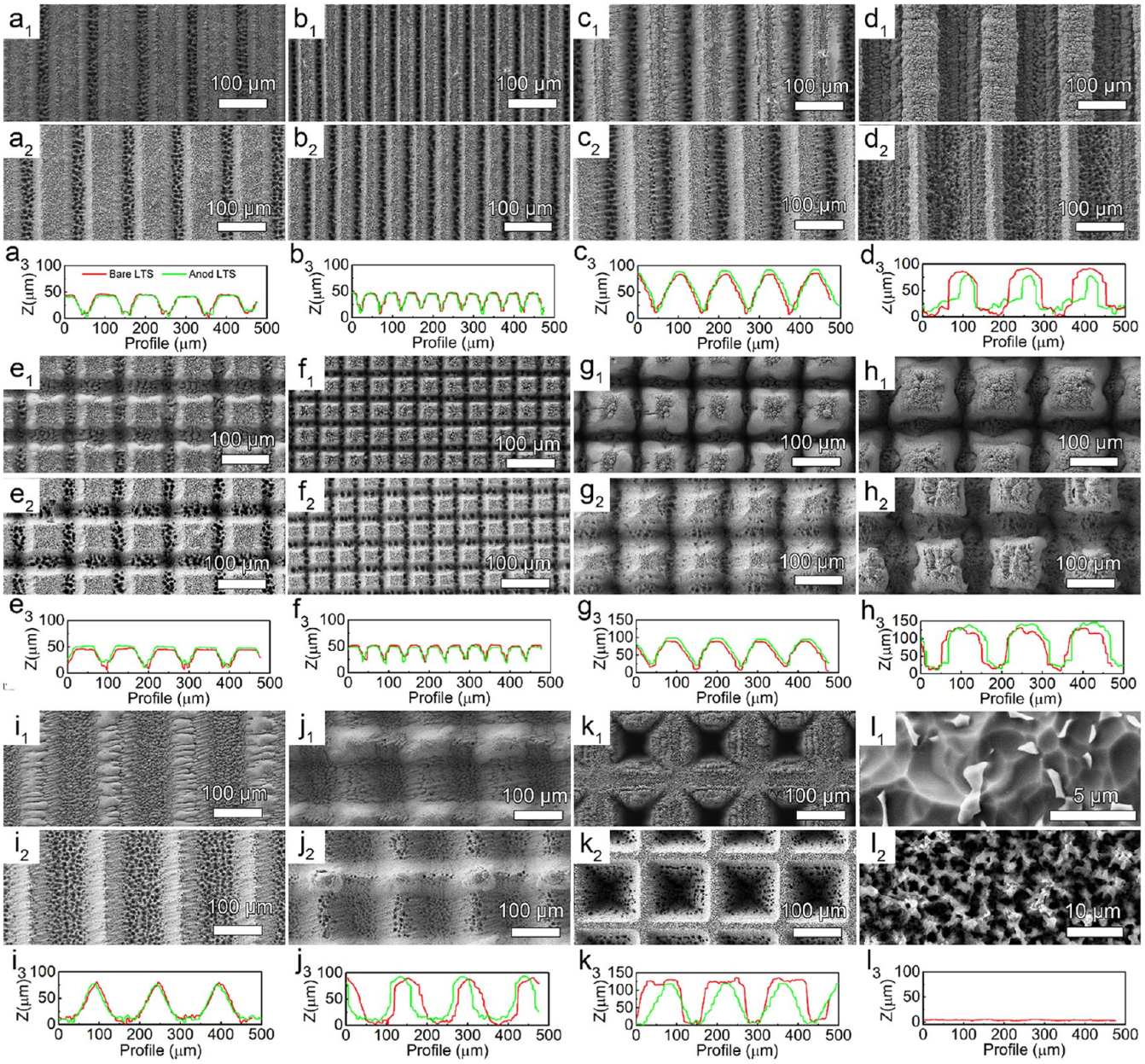

Figure 1. (a–k) Scanning electron microscopy (SEM) images and corresponding cross-sectional topography of laser-ablated titanium (Ti) alloy surfaces produced by infrared (IR) laser pulses. The structures vary from stripes (a–d, i), squares (e–h, j), and inverse pyramids (k). There are two surface treatments: (a_1–k_1) bare laser-treated samples, (a_2–k_2) laser-treated samples followed by electrochemical anodization, and (a_3–k_3) corresponding cross-sectional topography profiles. (l_1) SEM image of the as-manufactured Ti alloy surface. (l_2) An SEM image of an anodized Ti alloy surface without laser treatment. (l_3) Cross-sectional profile of the as-manufactured Ti alloy samples.

The dimensionless Wenzel roughness parameter for the bare Ti alloy surfaces was ∼1.0 (Figure 1l_3).

The as-produced Ti alloy surfaces are flat. Thus, the surfaces were treated with picosecond laser pulses to increase their roughness. This versatile technique allows for the creation of various structures in the order of tens of micrometers with high lateral resolution. The prepared patterns fall into three main categories: (i) parallel stripes (Figure 1a–d, i), (ii) corresponding squares (Figure 1e–h, j), and (iii) inverse pyramids (Figure 1k). The following laser irradiation parameters were employed and kept constant for all treatments: repetition rate (f) was set to 200 kHz; output laser power (P) was 4 W; and scanning speed (ν) was 40 mm s^{-1}. To decrease the solid–liquid area fraction in a controlled manner, linear and square patterns with five distinct size ratios between the ablated and nonablated areas were created. The distance between adjacent scan lines (hatch, H) and the number of rescans in the same area (N) were varied to achieve this (Figure S2). These parameters were varied as follows: (i) Stripe 1 and square 1, patterns were created with a hatch spacing of 100 μm and 13 repetitions of the line (Figures 1a_1,e_1, S1a,e, and S2a,e). The mean surface roughness of these substrates is 12.5 and 15.1 μm, with corresponding dimensionless Wenzel roughness parameters of 1.6 and 2.0, respectively, for stripe 1 and square 1 (Figure 1a_3,e_3). (ii) Stripe 2 and square 2 patterns were created with a hatch spacing of 50 μm and 13 repetitions (Figures 1b_1,f_1, S1b,f, and S2b,f). The mean surface roughness of these substrates is 10.0

https://doi.org/10.1021/acs.langmuir.5c05888
Langmuir 2026, 42, 8269–8279

μm for stripe 2 and 10.4 μm for square 2. The corresponding dimensionless Wenzel roughness parameters are 2.2 and 2.4, respectively (Figure 1b_3,f_3). (iii) A more complex laser-processing scheme was used to create stripe 3 and square 3. The laser scanning lines were arranged in groups of three with 16 μm of spacing between neighboring lines within each group. Each line was rescanned ten times consecutively before moving on to the next line in the group. The spacing between the outermost lines of neighboring groups was 44 μm, defining the interval between adjacent scan regions (Figures 1c_1,g_1, S1c,g, and S2c,g). The mean surface roughness of these substrates is 20.7 μm and 25.9 μm, respectively, with corresponding dimensionless Wenzel roughness parameters of 2.1 and 2.7 for stripe 3 and square 3 (Figure 1c_3,g_3). (iv) Stripe 4 and square 4 undergo laser processing similar to the previous case. However, the laser scanning lines are arranged in groups of 7, with 16 μm spacing between neighboring lines within each group. Each line was scanned ten times consecutively before moving on to the next line in the group (Figure 1d_1,h_1, S1d,h, and S2d,h). The spacing between the outermost lines of neighboring groups and the interval between adjacent scan regions remain similar to the previous case. The mean surface roughness of these substrates is 15.4 and 51.7 μm, respectively, with dimensionless Wenzel roughness parameters of 1.9 and 3.4 for stripe 4 and square 4 (Figure 1d_3,h_3). (v) In the laser processing of stripe 5 and square 5, scanning lines are grouped into sets of 7, with each line spaced 16 μm apart. Each line in the group is produced sequentially with 10 scans. The distance between the outermost lines of neighboring groups is 44 μm, defining the group spacing (Figures 1i_1–j_1, S1i–j, and S2i–j). The mean surface roughness of these substrates is 21.1 and 28.9 μm, respectively, with dimensionless Wenzel roughness parameters of 1.8 and 2.2 for stripe 5 and square 5 (Figure 1i_3–j_3). Finally, (vi) each inverse pyramid was formed by sequentially producing four overlapping squares with a single center of symmetry. The largest square had dimensions of 100 μm × 100 μm. Each subsequent dimension decreased by 20 μm until the final square's dimensions were 40 μm × 40 μm. The hatch distance for all squares was set to 10 μm, which is smaller than the laser spot radius. This ensured the uniform removal of the material inside the squares to a certain depth. Starting with the largest square, each square was scanned 4 times before moving on to the next smaller square. When spaced 150 μm apart along the x and y axes, the centers of the resulting neighboring inverse pyramids formed an array of inverted pyramids (Figures 1k_1, S1k, and S2k). These substrates have a mean surface roughness area of 21.0 μm and corresponding dimensionless Wenzel roughness parameters of 2.2 (Figure 1k_3).

Note that the intense laser irradiation rapidly heats the metal at the contact point. This leads to localized melting and vaporization of the material.[39] The vaporized metal and other debris produced during the laser processing are removed from the surface due to the pressure created by the rapid heating and expansion of the vapor. The removed material may consist of fine solid and liquid particles or a vapor plume. As the laser moves, the molten metal resolidifies on the surface, forming micrometer-rough grooves with round micro- and submicrometer features. These features are molten metal particles that partially coalesce before solidifying (Figure S1). To introduce nanoscale roughness and form hierarchical structures, the laser-treated surfaces (LTS) underwent electrochemical anodization in an aqueous electrolyte solution of $NaOH/H_2O_2$.[19] The surface morphologies of the anodized LTS samples are presented in Figures 1a_2–k_2 and S3a–k. As shown in (Figure 1a_2-k_2, and 1a_3-k_3), the anodized LTS samples preserve their LTS morphology and introduce randomly oriented, irregularly shaped, micrometer-scale protrusions. These protrusions have a subtle, nanoscale rough surface of anodized titanium oxide, which increases the overall surface roughness. The Wenzel roughness parameter increases from 1.6 to 2.0 for stripes 1 (Figures 1a and S3a), from 1.9 to 2.3 for squares 1 (Figures 1e and S3e), and from 2.2 to 2.9 for the inverse pyramid (Figures 1k and S3k). Note that measuring such hierarchically rough surfaces with high resolution remains challenging. A total of 23 surfaces with various hierarchical morphologies were produced and evaluated based on their solid–liquid area fraction and correlation with drop adhesive force.

Surface Functionalization Creates Cassie–Baxter Surfaces

Superhydrophobic surfaces require simultaneously increased surface roughness and a hydrophobic coating. Since laser-treated surfaces are hydrophilic due to the extensive presence of titanium oxide, the surfaces were exposed to a fluorinated phosphate ester surfactant (FS). *Note that poly- and perfluoroalkyl substances are subject to regulation due to their chemical stability, which may result in their bioaccumulation.*[40] Consequently, to minimize the waste of fluorinated compounds, the FS solution was utilized multiple times without any noticeable deterioration in coating performance for over 6 years.[29] The plain, anodized, and laser-treated Ti alloy samples were immersed in the FS solution at 60 °C for 30 min in an ambient atmosphere. Then, the samples were removed, washed with ethanol, and dried under a stream of compressed air. The resulting FS self-assembled monolayer was analyzed on the anodized and laser-treated samples using Fourier transform infrared (FTIR) spectroscopy, energy-dispersive X-ray spectroscopy (EDS), and X-ray photoelectron (XPS) spectroscopy (Figure 2).

We qualitatively analyzed the self-assembly of the FS surfactant using attenuated total reflectance Fourier-transform infrared (ATR-FTIR) spectroscopy on anodized Ti alloy samples (Figure 1l_2). Figure 2a presents the typical ATR-FTIR spectrum within the wavenumber range of 700–1500 cm^{-1}. Distinct peaks at 1,144 and 1,198 cm^{-1} are indicative of CF_2,[41,42] and the peak at 1,074 cm^{-1} is attributed to CF_3 stretching vibrations.[43] The shoulder at 1,237 cm^{-1} is attributed to P=O stretching vibrations of the FS molecule,[44] while the peak at 1006 cm^{-1} is assigned to the O–P–O bonds of the phosphate ester.[45] FTIR mapping and the corresponding spectra confirm the uniform chemical distribution of the FS monolayer on both the anodized and laser-treated Ti alloy surfaces (Figure 2b).

We further used EDS to analyze the chemical composition of the plain and FS-coated laser-treated samples. Figure 2c–e shows the typical EDS spectra and mapping for the laser-treated stripes before and after coating with the FS. Table S1 summarizes the results for all bare and anodized LTS surfaces. As Figure 2d, **e** shows, both samples are composed of the Ti6Al4V alloy, consisting of titanium (Ti), vanadium(V), and aluminum (Al). A pronounced oxygen peak is evident in the laser-treated samples with atomic concentrations higher than 49%, which is attributed to the laser treatment at ambient atmosphere (Table S1). Additionally, a distinct carbon peak with an atomic concentration ranging from 2.5% to 4.3% is

https://doi.org/10.1021/acs.langmuir.5c05888
Langmuir 2026, 42, 8269–8279

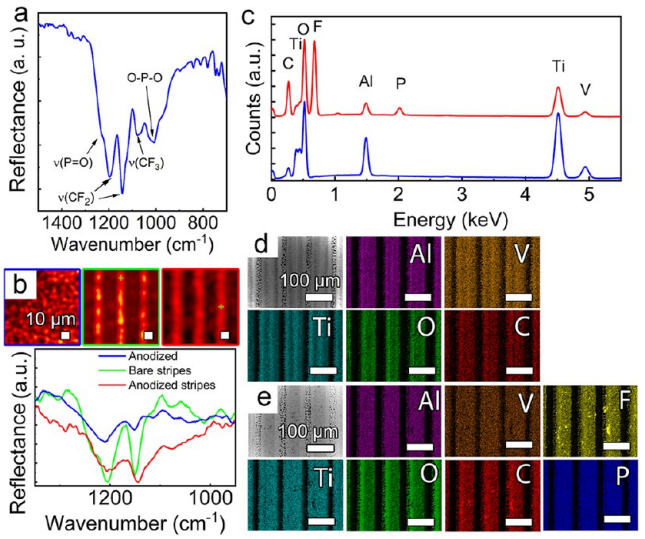

Figure 2. Chemical composition of the anodized and laser-treated Ti alloy samples. (a) ATR-FTIR spectrum of the FS self-assembled monolayer on the anodized Ti alloy sample. (b) Representative FTIR mapping and the corresponding spectra of the FS coverage of the anodized and LTS stripe surfaces at a wavenumber of 1,210 cm^{-1}. (c–e) EDS pattern and corresponding maps of the as-formed (blue line in (c)) and FS self-assembled monolayer (red line in (c)) of laser-treated stripe samples.

evident. The presence of phosphorus (P) and fluorine (F) peaks is also evident in the FS-coated bare and anodized laser-treated samples, even with a monolayer of FS (Figure 2c and Table S2). This is due to the increased surface area characteristic of the laser-treated sample morphology.

Prospective applications of SHS require long-term wetting performance in both air and water. Several recent studies have reported the fabrication of metallic superhydrophobic surfaces exclusively through laser treatment.[46,47] It was observed that the as-formed laser-treated samples were initially superhydrophilic but became superhydrophobic upon aging in air. This phenomenon was attributed to a chemical interaction between the surface and ambient CO_2, which was amplified by nanostructures. An accumulation of carbon and its compounds resulted in the laser-treated surfaces.[48] However, this hypothesis was largely speculative as the wetting characteristics were not supported by chemical analysis. Therefore, XPS was used to quantitatively analyze the elemental composition and chemical state of the elements present on the laser-treated surfaces.

Survey and high-resolution XPS spectra of Ti alloy laser-treated samples in stripe or square configurations exhibit characteristic peaks for C, O, N, Ti, Al, and V (Figures 3a–e, S4, and Table S3). The aged laser-treated samples exhibit a higher C 1s peak intensity (Figure 3b). The C 1s peak is centered at ≈284.8 eV in both cases, which indicates adventitious carbon (C–C and C–H bonds) adsorbed on the surface (Figure 3b).[49] Note that the aged laser-treated samples have an increased C 1s peak intensity, corresponding to a 2-fold increase in the C atomic concentration (Figure 3b and Table S3). To determine whether these findings are due to

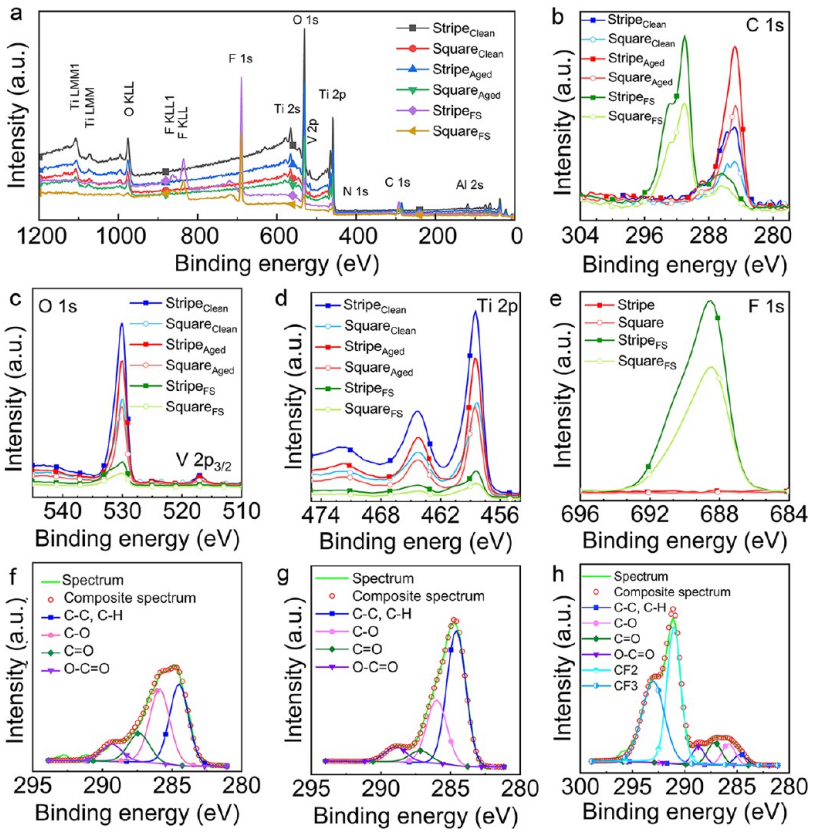

Figure 3. (a) Survey and (b–e) high-resolution XPS spectra of the as-formed, in an ambient atmosphere aged, and FS-coated laser-treated samples with striped and square morphologies: (b) C 1s, (c) O 1s, (d) Ti 2p, and (e) F 1s peaks. (f–h) Fitting of the C 1s peak for the (f) as-formed, (g) aged, and (h) FS-coated laser-treated samples.

https://doi.org/10.1021/acs.langmuir.5c05888
Langmuir 2026, 42, 8269–8279

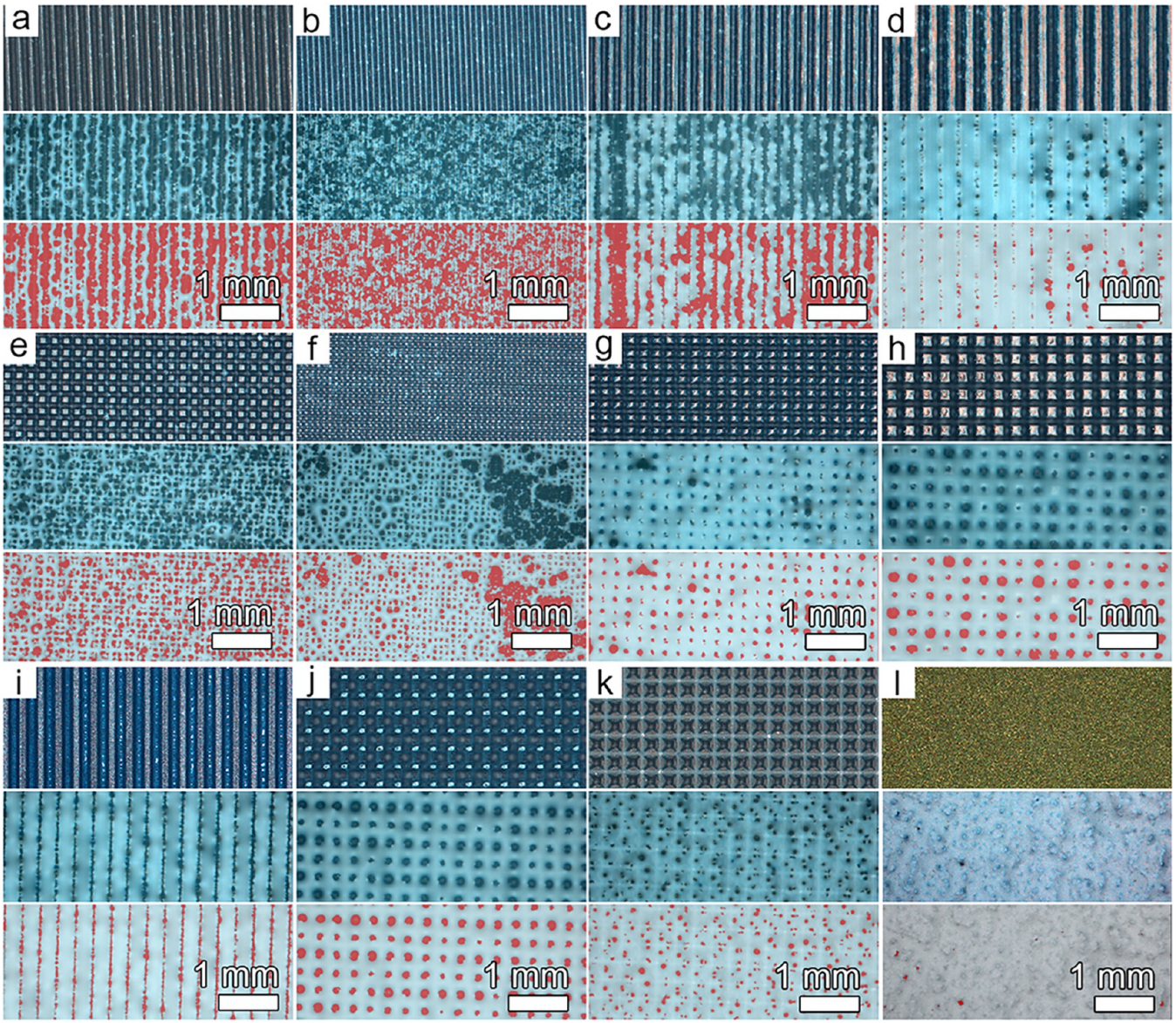

Figure 4. Solid–liquid area fraction was calculated from optical reflectance microscopy images of the FS-coated laser-treated Ti alloy samples immersed in water: (a–d, **i**) Stripe 1–4, and 5, (e–h, j) Squares 1–4, and 5, (k) Inverse pyramids, and (l) anodized Ti alloy samples without laser treatment. Each image shows the sample surface measured in air (top images), the same sample imaged underwater (middle images), and the calculated solid–liquid area fraction masked in red (bottom images). The scale bar is equal for all images.

contamination, we fitted the C 1s peak for the as-formed and aged laser-treated samples (Figure 3f,g). The results confirm the following: (i) the as-formed LTS samples possess a small amount of carbon contamination (with C–C/C-H at 285.5 eV, C–O at 285.9 eV, C═O at 287.4 eV, and O–C═O at 289.3 eV),[50,51] and (ii) aging leads to additional carbon uptake from the environment as evidenced by the absence of a C–Ti bond at 281 eV.[52] This suggests that there is no obvious chemical interaction between the laser-treated surface and ambient CO_2, and that washing in ethanol effectively removes physisorbed contaminants, thereby restoring the aged laser-treated samples to their original hydrophilic wetting state.[53] Thus, to ensure long-term wetting-repellent performance, the as-formed laser-treated surfaces should be chemically modified with a low-energy compound, such as FS.

Following the FS treatment, a high-intensity C 1s peak centered at 291.0 eV and a prominent shoulder at 293.0 eV are observed in the spectra, which are indicative of CF_2 and CF_3 bonds, respectively. Additionally, a clear F 1s peak is observed at 688.5 eV (Figure 3b) as well as a P 2p peak at 134.3 eV (Figure S4b).[50] Concurrently, the intensity of the Ti 2p and O 1s peaks decreased for the FS-coated laser-treated samples due to the FS molecule (Figure 3c,d). Based on the C 1s peak fitting for the FS-coated laser-treated samples (Figure 3h) and the broadness of the F 1s peak, meaning F is in CF_2 at ≈ 688.5 eV and in CF_3 at ≈ 690.5 eV (Figure 3e), the orientation of the molecules on the FS-coated laser-treated surfaces shows higher CF_3 bond intensity than expected. The usual CF_3:CF_2 ratio is 1:5 to 1:9.[29] Here, the CF_3:CF_2 area ratio from peak fitting indicates that CF_2 has 41% of the area and CF_3 39%, *i.e.*, almost a 1:1 ratio, which is attributed to the high roughness of the laser-treated samples.

https://doi.org/10.1021/acs.langmuir.5c05888
Langmuir 2026, 42, 8269–8279

The Solid−Liquid Area Fraction was Calculated Using Optical Reflectance Microscopy Images

The solid−liquid area fraction is the ratio of the area of the solid surface in contact with a liquid to the plastron area. This ratio was calculated directly from optical reflectance microscopy images of bare and anodized laser-treated samples covered by an FS self-assembly monolayer while immersed underwater, and the results are summarized in Figure 4 for the bare laser-treated surfaces, Figure S5 for the anodized laser-treated surfaces, and Table S4. For comparison, the same surfaces are displayed as measured in air using the same reflectance optical microscopy (Figures 4 and S5, top images). The stripe, square, and inverse-pyramid laser-treated morphologies are clearly observable on the sample surfaces in air. However, when immersed underwater, only the tops of these structures partially contact the surrounding liquid, appearing as dark spots in the images (Figures 4 and S5, middle images). Meanwhile, the grooves remain filled with air and appear as bright, smooth areas in the optical images (Figures 4 and S5, middle images). The color change makes it easier to calculate the SLAF on surfaces immersed in water where the SLAF is masked by a red color (Figures 4 and S5, bottom images). Using laser treatment procedures with and without subsequent anodization allows us to precisely control a fraction of the solid−liquid area (Figures 4a−k and S5). The laser-treated samples demonstrated solid−liquid area fraction values ranging from 7.1% ± 0.4% to 49.3% ± 3.9%. For comparison, we used as-anodized Ti alloy samples without laser treatment that exhibited a value of 0.1% ± 0.1%, meaning that almost 99.9% of the area is covered by plastron (Figure 4l).[19]

Drop Adhesive Force Measurements and Their Correlation with the Solid−Liquid Area Fraction

Figure 5a (also see Figure S6, Movie S3, and Section S11 in Supporting Information) presents a typical drop adhesive force measurement for adhesive samples with a solid−liquid area fraction of ∼85%, that is, the surface is mainly in the Wenzel wetting state. The drop adhesive force experiment includes several distinct steps: (i) The sample surface approaches a drop of a specific volume on the needle tip (Figure 5a, step 1). (ii) The sample continues to move up a predefined distance, compressing the drop. This results in an increase in interaction force and a negative value (Figure 5a, step 2). During this step, the three-phase contact line moves outward, corresponding to the advancing CAs. (iii) The surface remains at the maximum compression for a duration of 1 s, allowing sufficient time for wetting. (iv) The sample surface moves down, stretching the drop. During this step, the interaction force first reduces to zero and then increases to the greatest positive drop adhesive force value (Figure 5a, step 3). The three-phase contact line moves inward, corresponding to the receding CAs. (v) After that point, the surface continues moving down until the drop separates from the needle (tear-off) (Figure 5a, step 4). To exclude the influence of the drop size on the measured drop adhesive force, the total measured adhesive force was normalized by the contact circumference of the drop on the surface.

The drop adhesive force procedure was applied to the bare and anodized laser-treated samples that were coated with FS. The results are summarized in Figure 5b−e. All laser-treated samples exhibited low adhesion to water drops, and the tear-off event was not observed (*i.e.*, the drop remained entirely on the needle). Also, all Cassie−Baxter superhydrophobic surfaces

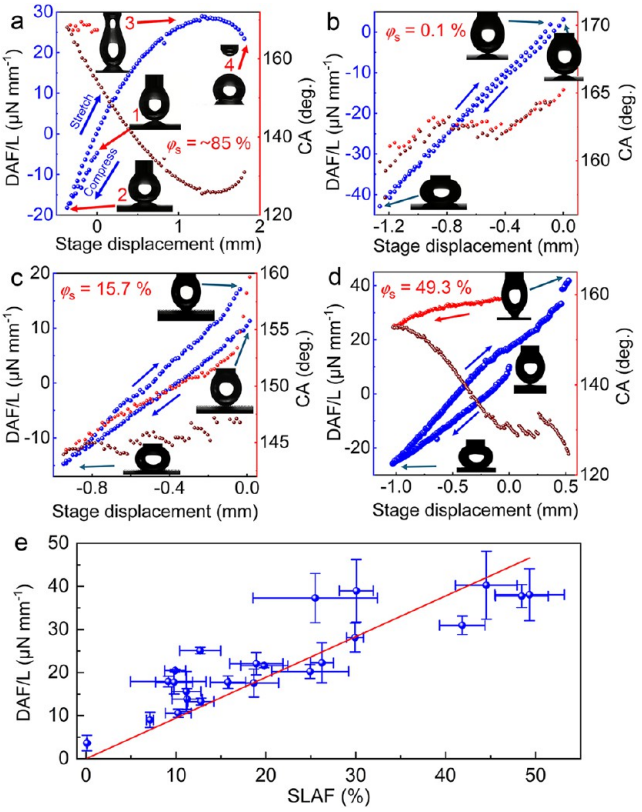

Figure 5. Typical drop adhesive force curve and corresponding water contact angles (CAs) for (a) high values of solid−liquid area fraction, (b) 0.1%, (c) 15.7%, and (d) 49.3%. (e) Correlation between the drop adhesive force and the solid−liquid area fraction of superhydrophobic surfaces. The bright red dots in (a−d) represent the calculated contact angle values during the compressing drop step, while the dark red (brownish) dots correspond to contact angles during the stretching drop step. The error in (e) for the drop adhesive force is the standard deviation of the force data calculated on the corresponding sample as the average over at least 3 independent measurements, and the error for the solid−liquid area fraction is the standard deviation of the solid−liquid area fraction calculated on the corresponding sample as the average over at least 3 independent measurements.

demonstrate nontypical drop adhesive force curves. In the control samples with the lowest solid−liquid area fraction values, the compression and stretching lines almost completely overlap, indicating extremely low CA hysteresis values (Figure 5b). Consequently, the drop adhesive force value on these surfaces remains at an exceptionally low level, thereby confirming the low water adhesion due to the presence of an almost continuous plastron. It should be noted that in these samples, the typical drop adhesive maximum value was not observed, as shown in Figure 5a by point 3; thus, we consider the highest measured positive force value as the drop adhesive force.

An increase in solid−liquid area fraction values results in higher drop adhesive force and, thus, contact angle hysteresis values, due to an increased number of pinning states (Figure 5c,d). Figure 5e summarizes the drop adhesive force calculations as a function of the solid−liquid area fraction over all 23 developed surfaces in the Cassie−Baxter wetting state. As shown, the dependence is nearly linear, with a fitted linear regression slope of 94.4 ± 4.9 μN mm^{-1} (R^2 = 0.94) (see also Figure S7). It is worth noting that the fabrication of

https://doi.org/10.1021/acs.langmuir.5c05888
Langmuir 2026, 42, 8269−8279

structures with characteristic lateral dimensions on the order of tens to hundreds of microns by laser ablation, while achieving uniform micro- and nanoscale roughness along their edges, remains challenging.[54] The combination of high energy density and multiple pulses with the material-specific nominal surface topography and chemical composition (Ti alloy) leads to dynamic changes in the material removal mechanisms, resulting in a relatively wide variation in microscale roughness across the entire ablated surface and, particularly, at the structure's boundaries.[55] This effect impacts the SLAF values, leading to their standard deviations, even at the same pattern (Figure 5e). The latter also affects the electrochemical anodization step.

Our DAF-SLAF result is significant because such a simple experiment can predict the relationship between the drop adhesive force and its corresponding solid−liquid area fraction of the Cassie−Baxter surface. Insights derived from this correlation will guide the development of new surfaces and coatings with tailored solid−liquid area fraction by optimizing surface texture to achieve the desired degree of wetting-repellent performance. Additionally, due to the significant uncertainty in goniometric measurements, it is crucial to understand the correlation between drop adhesive forces and solid−liquid area fraction for effectively designing, implementing, and innovating Cassie−Baxter superhydrophobic surfaces across various fields.

CONCLUSIONS

This study presents a novel and straightforward approach to quantifying the solid−liquid area fraction of the air layer trapped on Cassie−Baxter superhydrophobic surfaces. The current state-of-the-art in characterizing SHS is based on wetting parameters, such as the apparent contact angle (CA) and CA hysteresis. While these measurements are easily accessible, they are difficult to interpret for several reasons. From an experimental point of view, the apparent CA is a combination of surface roughness and the chemical homogeneity of the low-energy coating; thus, the contribution of each component must be deconvoluted. However, measuring surface roughness on hierarchical structures with high precision is challenging, even with up-to-date tools such as atomic force and laser confocal microscopes. Additionally, analyzing surface coverage by a low-energy coating, whether homogeneous or not, is not a common practice. From a computational perspective, the algorithms used to calculate advancing and receding contact angles and consequently CA hysteresis may produce significant deviations.[56] Measurement errors may derive from various factors, including substrate characteristics, optical limitations, and image resolution. As previously demonstrated, three-phase contact line adjustments can also lead to significant errors in apparent CA calculations.[11] Furthermore, in practice, the value of the apparent CA value depends on how a drop lands on a solid surface. In the Gibbs free energy landscape, a water drop can stabilize at any local minimum between the advancing and receding CAs because the drop-landing process involves random elements.[4] Finally, goniometric measurements provide information about neither the stability of the wetting state nor the plastron formed.

We recently proposed an effective method for measuring the solid−liquid area fraction of trapped air on Cassie−Baxter superhydrophobic surfaces. This method uses optical reflectance microscopy and has been demonstrated to work well on surfaces with high plastron coverage and low surface reflectance.[3,19] It provides a millimeter field of view with micrometer lateral resolution. This is particularly significant because surfaces with similar superhydrophobic properties according to goniometric measurements can have substantial variations in their wetting-repellent performance.[14] To simplify and standardize these measurements, we demonstrate the correlation between the drop adhesive force and solid−liquid area fraction. To achieve this, we coated laser-treated and laser-treated/anodized surfaces with a fluorinated surfactant, which resulted in a gradual change in their solid−liquid area fraction values. All laser-treated samples exhibited low adhesion to water drops. Drops of 10 μL did not adhere to these surfaces, making the measurement of an apparent contact angle impractical. Here, we demonstrate that the drop adhesive force correlates linearly with solid−liquid area fraction. This simple methodology enables the rapid assessment of superhydrophobic surfaces in the Cassie−Baxter state and facilitates the prediction of plastron coverage. It also helps identify the most promising candidates even before measuring more challenging parameters, such as Wenzel roughness, solid−liquid area fraction, and various CAs. This is significant for investigating the wetting-repellent performance of superhydrophobic surfaces because properties such as corrosion resistance, biofouling resistance, ice adhesion, and friction-free floating depend directly on solid−liquid area fraction.

ASSOCIATED CONTENT

Data Availability Statement

The data that support the findings of this study are available from the corresponding author upon reasonable request.

Supporting Information

The Supporting Information is available free of charge at https://pubs.acs.org/doi/10.1021/acs.langmuir.5c05888.

(1) High-magnification SEM images of bare LTS surfaces, (2) Schematic representation of laser structuring procedures, (3) High-magnification SEM images of anodized LTS surfaces, (4) Atomic percentages of bare and anodized LTS Samples Measured by Energy-Dispersive X-ray spectroscopy, (5) Atomic percentages of bare and FS-coated LTS samples measured by energy-dispersive X-ray spectroscopy, (6) Atomic concentration of elements measured by XPS on as-formed, aged, and FS-coated Ti alloy samples, (7) High-resolution XPS spectra of P 2p, N 1s, and Al 2p peaks measured on as-formed, aged, and FS-treated LTS, (8) Calculated solid−liquid area fraction using optical reflectance microscopy images on anodized LTS samples, (9) Adhesive force measurement correlated with SLAF on a bare Ti alloy sample covered by the FS surfactant, (10) Correlation between the DAF and the SLAF of SHS as a function of surface treatment, and (11) Theoretical background of DAF measurements (PDF)

The 5 and 10 μL drop volume adhesiveness measured on the Cassie−Baxter superhydrophobic sample with ∼50% solid−liquid area fraction (Video S1) (MP4)

The 30 μL volume drop adhesive force experiment measured on the Cassie−Baxter superhydrophobic samples with 0.1%, 16%, and ∼50% solid−liquid area fraction (Video S2) (WMV)

https://doi.org/10.1021/acs.langmuir.5c05888
Langmuir 2026, 42, 8269−8279

The 30 μL volume drop adhesive force experiment measured on the sample with 85% solid−liquid area fraction (Video S3) (MP4)

AUTHOR INFORMATION

Corresponding Author

Alexander B. Tesler − *Department of Physics Biophysics Group, Friedrich-Alexander-Universität Erlangen-Nürnberg, 91052 Erlangen, Germany; Department of Materials Engineering, Faculty of Engineering, Bar Ilan University, Ramat-Gan 5290002, Israel;* orcid.org/0000-0003-3425-7667; Email: alexander.tesler@biu.ac.il

Authors

Petr Druzhinin − *Institute for Nanotechnology and Correlative Microscopy gGmbH (INAM), 91301 Forchheim, Germany; Fraunhofer Institute for Ceramic Technologies and Systems IKTS, 91301 Forchheim, Germany*

Iana Fomicheva − *Fraunhofer Institute for Ceramic Technologies and Systems IKTS, 91301 Forchheim, Germany; Department of Physics, Friedrich-Alexander-Universität Erlangen-Nürnberg, 91058 Erlangen, Germany*

George Sarau − *Institute for Nanotechnology and Correlative Microscopy gGmbH (INAM), 91301 Forchheim, Germany; Fraunhofer Institute for Ceramic Technologies and Systems IKTS, 91301 Forchheim, Germany; Max Planck Institute for the Science of Light, 91058 Erlangen, Germany*

Anca Mazare − *Department of Materials Science, Institute for Surface Science and Corrosion, Friedrich-Alexander-Universität Erlangen-Nürnberg, 92058 Erlangen, Germany*

Bihai Song − *Ningbo NB Scientific Instruments Co., Ltd, Ningbo City 315048, China*

Wolfgang H. Goldmann − *Department of Physics Biophysics Group, Friedrich-Alexander-Universität Erlangen-Nürnberg, 91052 Erlangen, Germany;* orcid.org/0000-0003-0738-2665

Silke H. Christiansen − *Institute for Nanotechnology and Correlative Microscopy gGmbH (INAM), 91301 Forchheim, Germany; Fraunhofer Institute for Ceramic Technologies and Systems IKTS, 91301 Forchheim, Germany; Physics Department, Freie Universität Berlin, 14195 Berlin, Germany;* orcid.org/0000-0002-4908-4087

Complete contact information is available at: https://pubs.acs.org/10.1021/acs.langmuir.5c05888

Author Contributions

¶P.D. and I.F. contributed equally to this work.

Notes

The authors declare no competing financial interest.

ACKNOWLEDGMENTS

I.F., A.B.T., and W.H.G. thank the Deutsche Forschungsgemeinschaft (DFG) for financial support (award number 540989797). I.F., G.S., and S.C. were supported by the European Union's H2020 research and innovation program through the Marie Sklodowska-Curie grant agreement AIMed ID: 861138, the research projects 4D+ nanoSCOPE ID: 810316 and LRI ID: C10, STOP ID: 101057961, and the German Research Foundation (DFG) within the research project UNPLOK ID: 523847126, and from the "Freistaat Bayern" and the European Union within the project Analytiktechnikum für Gesundheits- und Umweltforschung AGEUM, project (StMWi-43-6623-22/1/3). The authors thank Mr. Matti Duschek from LAUDA Scientific GmbH for providing the instrument to measure drop adhesive forces.

REFERENCES

(1) Quéré, D. Wetting and Roughness. *Annu. Rev. Mater. Res.* **2008**, *38*, 71−99.

(2) Kolle, S.; Davitt, A.; Zhou, Y.; Aizenberg, J.; Adera, S. Synergistic Benefits of Micro/Nanostructured Oil-Impregnated Surfaces in Reducing Fouling while Enhancing Heat Transfer. *Langmuir* **2023**, *39* (19), 6705−6712.

(3) Tesler, A. B.; Nurmi, H. A.; Kolle, S.; Prado, L. H.; Karunakaran, B.; Mazare, A.; Erceg, I.; de Brito Soares, Í.; Sarau, G.; Christiansen, S.; Stafslien, S.; Alvarenga, J.; Aizenberg, J.; Fabry, B.; Ras, R. H. A.; Goldmann, W. H. Predicting plastron thermodynamic stability for underwater superhydrophobicity. *Commun. Mater.* **2024**, *5* (1), No. 112.

(4) Marmur, A.; Volpe, C. D.; Siboni, S.; Amirfazli, A.; Drelich, J. W. Contact angles and wettability: towards common and accurate terminology. *Surf. Innov.* **2017**, *5* (1), 3−8.

(5) Butt, H.-J.; Liu, J.; Koynov, K.; Straub, B.; Hinduja, C.; Roismann, I.; Berger, R.; Li, X.; Vollmer, D.; Steffen, W.; Kappl, M. Contact angle hysteresis. *Curr. Opin. Colloid Interface Sci.* **2022**, *59*, No. 101574.

(6) Dong, Z.; Vuckovac, M.; Cui, W.; Zhou, Q.; Ras, R. H. A.; Levkin, P. A. 3D Printing of Superhydrophobic Objects with Bulk Nanostructure. *Adv. Mater.* **2021**, *33* (45), No. 2106068.

(7) Parvate, S.; Dixit, P.; Chattopadhyay, S. Superhydrophobic Surfaces: Insights from Theory and Experiment. *J. Phys. Chem. B* **2020**, *124* (8), 1323−1360.

(8) Si, Y.; Dong, Z.; Jiang, L. Bioinspired Designs of Superhydrophobic and Superhydrophilic Materials. *ACS Cent. Sci.* **2018**, *4* (9), 1102−1112.

(9) Li, L.; Wei, J.; Zhang, J.; Li, B.; Yang, Y.; Zhang, J. Challenges and strategies for commercialization and widespread practical applications of superhydrophobic surfaces. *Sci. Adv.* **2023**, *9* (42), No. eadj1554.

(10) Drelich, J. W. Contact angles: From past mistakes to new developments through liquid-solid adhesion measurements. *Adv. Colloid Interface Sci.* **2019**, *267*, 1−14.

(11) Liu, K.; Vuckovac, M.; Latikka, M.; Huhtamäki, T.; Ras, R. H. A. Improving surface-wetting characterization. *Science* **2019**, *363* (6432), 1147−1148.

(12) Vuckovac, M.; Latikka, M.; Liu, K.; Huhtamäki, T.; Ras, R. H. A. Uncertainties in contact angle goniometry. *Soft Matter* **2019**, *15* (35), 7089−7096.

(13) Lafuma, A.; Quéré, D. Superhydrophobic states. *Nat. Mater.* **2003**, *2* (7), 457−460.

(14) Prado, L. H.; Hayek, S.; Mazare, A.; Erceg, I.; Sarau, G.; Christiansen, S.; Kamaleev, M.; Wurmshuber, M.; Lohbauer, U.; Goldmann, W. H.; Virtanen, S.; Tesler, A. B. Aerophilic Surfaces for Sustained Corrosion Protection of Metals Underwater. *Adv. Funct. Mater.* **2024**, *34* (44), No. 2407444.

(15) Poetes, R.; Holtzmann, K.; Franze, K.; Steiner, U. Metastable Underwater Superhydrophobicity. *Phys. Rev. Lett.* **2010**, *105* (16), No. 166104.

(16) Röhrig, M.; Mail, M.; Schneider, M.; Louvin, H.; Hopf, A.; Schimmel, T.; Worgull, M.; Hölscher, H. Nanofur for Biomimetic Applications. *Adv. Mater. Interfaces* **2014**, *1* (4), No. 1300083.

(17) Mehanna, Y. A.; Sadler, E.; Upton, R. L.; Kempchinsky, A. G.; Lu, Y.; Crick, C. R. The challenges, achievements and applications of submersible superhydrophobic materials. *Chem. Soc. Rev.* **2021**, *50* (11), 6569−6612.

(18) Martínez-Gómez, A.; López, S.; García, T.; de Francisco, R.; Tiemblo, P.; García, N. Long-Term Underwater Hydrophobicity: Exploring Topographic and Chemical Requirements. *ACS Omega* **2017**, *2* (12), 8928−8939.

(19) Tesler, A. B.; Kolle, S.; Prado, L. H.; Thievessen, I.; Böhringer, D.; Backholm, M.; Karunakaran, B.; Nurmi, H. A.; Latikka, M.; Fischer, L.; Stafslien, S.; Cenev, Z. M.; Timonen, J. V. I.; Bruns, M.; Mazare, A.; Lohbauer, U.; Virtanen, S.; Fabry, B.; Schmuki, P.; Ras, R. H. A.; Aizenberg, J.; Goldmann, W. H. Long-Lasting Aerophilic Metallic Surfaces Underwater. *Nat. Mater.* **2023**, *22* (12), 1548−1555.
(20) Fomicheva, I.; Druzhinin, P.; Pavlovska, M.; Ferner, K.; Frese, D.; Sarau, G.; Mazare, A.; Goldmann, W. H.; Fabry, B.; Christiansen, S.; Tesler, A. B. Advanced Characterization of Plastron on Cassie-Baxter Superhydrophobic Surfaces by Drop Adhesion Forces.
(21) Butt, H.-J.; Roisman, I. V.; Brinkmann, M.; Papadopoulos, P.; Vollmer, D.; Semprebon, C. Characterization of super liquid-repellent surfaces. *Curr. Opin. Colloid Interface Sci.* **2014**, *19* (4), 343−354.
(22) Nagy, N. Contact Angle Determination on Hydrophilic and Superhydrophilic Surfaces by Using r−θ-Type Capillary Bridges. *Langmuir* **2019**, *35* (15), 5202−5212.
(23) Nagy, N. Capillary Bridges on Hydrophobic Surfaces: Analytical Contact Angle Determination. *Langmuir* **2022**, *38* (19), 6201−6208.
(24) Reyssat, M.; Quéré, D. Contact Angle Hysteresis Generated by Strong Dilute Defects. *J. Phys. Chem. B* **2009**, *113* (12), 3906−3909.
(25) Qiao, S.; Li, S.; Li, Q.; Li, B.; Liu, K.; Feng, X.-Q. Friction of Droplets Sliding on Microstructured Superhydrophobic Surfaces. *Langmuir* **2017**, *33* (47), 13480−13489.
(26) Zhang, S.; Zhao, L.; Yu, M.; Guo, J.; Liu, C.; Zhu, C.; Zhao, M.; Huang, Y.; Zheng, Y. Measurement Methods for Droplet Adhesion Characteristics and Micrometer-Scale Quantification of Contact Angle on Superhydrophobic Surfaces: Challenges and Opportunities. *Langmuir* **2024**, *40* (19), 9873−9891.
(27) Backholm, M.; Molpeceres, D.; Vuckovac, M.; Nurmi, H.; Hokkanen, M. J.; Jokinen, V.; Timonen, J. V. I.; Ras, R. H. A. Water droplet friction and rolling dynamics on superhydrophobic surfaces. *Commun. Mater.* **2020**, *1* (1), No. 64.
(28) Tan, Y.; Yang, J.; Li, Y.; Li, X.; Wu, Q.; Fan, Y.; Yu, F.; Cui, J.; Chen, L.; Wang, D.; Deng, X. Liquid-Pressure-Guided Superhydrophobic Surfaces with Adaptive Adhesion and Stability. *Adv. Mater.* **2022**, *34* (30), No. 2202167.
(29) Timonen, J. V. I.; Latikka, M.; Ikkala, O.; Ras, R. H. A. Free-decay and resonant methods for investigating the fundamental limit of superhydrophobicity. *Nat. Commun.* **2013**, *4* (1), No. 2398.
(30) Zhang, Y.; Wang, T.; Lv, Y. Durable Biomimetic Two-Tier Structured Superhydrophobic Surface with Ultralow Adhesion and Effective Antipollution Property. *Langmuir* **2023**, *39* (7), 2548−2557.
(31) Nagy, N. Determination of solid-liquid adhesion work on flat surfaces in a direct and absolute manner. *Sci. Rep.* **2024**, *14* (1), No. 29991.
(32) Lepikko, S.; Turkki, V.; Koskinen, T.; Raju, R.; Jokinen, V.; Kiseleva, M. S.; Rantataro, S.; Timonen, J. V. I.; Backholm, M.; Tittonen, I.; Ras, R. H. A. Droplet Friction on Superhydrophobic Surfaces Scales With Liquid-Solid Contact Fraction. *Small* **2025**, *21* (7), No. 2405335.
(33) Liimatainen, V.; Vuckovac, M.; Jokinen, V.; Sariola, V.; Hokkanen, M. J.; Zhou, Q.; Ras, R. H. A. Mapping microscale wetting variations on biological and synthetic water-repellent surfaces. *Nat. Commun.* **2017**, *8* (1), No. 1798.
(34) Srinivasan, S.; McKinley, G. H.; Cohen, R. E. Assessing the Accuracy of Contact Angle Measurements for Sessile Drops on Liquid-Repellent Surfaces. *Langmuir* **2011**, *27* (22), 13582−13589.
(35) Wang, F.; Zhang, H.; Nestler, B. Wetting Phenomena: Line Tension and Gravitational Effect. *Phys. Rev. Lett.* **2024**, *133* (24), No. 246201.
(36) Butt, H.-J.; Kappl, M. Normal capillary forces. *Adv. Colloid Interface Sci.* **2009**, *146* (1), 48−60.
(37) Song, B.; Springer, J. Determination of Interfacial Tension from the Profile of a Pendant Drop Using Computer-Aided Image Processing: 1. Theoretical. *J. Colloid Interface Sci.* **1996**, *184* (1), 64−76.
(38) Marmur, A. Underwater Superhydrophobicity: Theoretical Feasibility. *Langmuir* **2006**, *22* (4), 1400−1402.
(39) Brown, M. S.; Arnold, C. B. Fundamentals of Laser-Material Interaction and Application to Multiscale Surface Modification. In *Laser Precision Microfabrication*; Sugioka, K.; Meunier, M.; Piqué, A., Eds.; Springer Berlin Heidelberg, 2010; pp 91−120.
(40) Cousins, I. T.; Johansson, J. H.; Salter, M. E.; Sha, B.; Scheringer, M. Outside the Safe Operating Space of a New Planetary Boundary for Per- and Polyfluoroalkyl Substances (PFAS). *Environ. Sci. Technol.* **2022**, *56* (16), 11172−11179.
(41) Claves, D. Spectroscopic study of fluorinated carbon nanostructures. *New J. Chem.* **2011**, *35* (11), 2477−2482.
(42) Ignatieva, L. N.; Mashchenko, V. A.; Zverev, G. A.; Ustinov, A. Y.; Slobodyuk, A. B.; Bouznik, V. M. Study of the manufactured copolymers of ethylene with tetrafluoroethylene. *J. Fluor. Chem.* **2020**, *231*, No. 109460.
(43) Milligan, D. E.; Jacox, M. E. Matrix-Isolation Study of the Reaction of Atomic and Molecular Fluorine with Carbon Atoms. The Infrared Spectra of Normal and ^{13}C-Substituted CF_2 and CF_3. *J. Chem. Phys.* **1968**, *48* (5), 2265−2271.
(44) Withnall, R.; Andrews, L. Infrared spectra of oxygen atom-phosphine reaction products trapped in solid argon. *J. Phys. Chem. A* **1988**, *92* (16), 4610−4619.
(45) Bourbigot, S.; Le Bras, M.; Delobel, R.; Trémillon, J.-M. Synergistic effect of zeolite in an intumescence process. Study of the interactions between the polymer and the additives. *J. Chem. Soc., Faraday Trans.* **1996**, *92* (18), 3435−3444.
(46) Kietzig, A.-M.; Hatzikiriakos, S. G.; Englezos, P. Patterned Superhydrophobic Metallic Surfaces. *Langmuir* **2009**, *25* (8), 4821−4827.
(47) Kietziga, A.-M.; Mirvakilia, M. N.; Kamalb, S.; Englezosa, P.; Hatzikiriakosa, S. G. Nanopatterned Metallic Surfaces: Their Wettability and Impact on Ice Friction. *J. Adhes. Sci. Technol.* **2011**, *25* (12), 1293−1303.
(48) Vorobyev, A. Y.; Guo, C. Multifunctional surfaces produced by femtosecond laser pulses. *J. Appl. Phys.* **2015**, *117* (3), No. 033103.
(49) Grey, L. H.; Nie, H.-Y.; Biesinger, M. C. Defining the nature of adventitious carbon and improving its merit as a charge correction reference for XPS. *Appl. Surf. Sci.* **2024**, *653*, No. 159319.
(50) Mazare, A.; Ulubas, M. H.; Kim, H.; Fomicheva, I.; Sarau, G.; Christiansen, S. H.; Goldmann, W. H.; Tesler, A. B. Binding Kinetics of Self-Assembled Monolayers of Fluorinated Phosphate Ester on Metal Oxides for Underwater Aerophilicity. *Langmuir* **2025**, *41* (3), 1868−1875.
(51) Wanger, C.; Riggs, W.; Davis, L.; Moulder, J.; Muilenberg, G. *Handbook of X-ray Photoelectron Spectroscopy: A Reference Book of Standard Data for Use in X-ray Photoelectron Spectroscopy.*; Physical Electronics Division, Perkin-Elmer Corp: Eden Prairie, MN, 1979.
(52) Sheu, B. R.; Strongin, D. R. Adsorption and thermal decomposition of methanol on 3d transition metal (iron, nickel, titanium) aluminides: FeAl(110), NiAl, and TiAl. *J. Phys. Chem. A* **1993**, *97* (39), 10144−10151.
(53) Park, J.; Tesler, A. B.; Gongadze, E.; Iglič, A.; Schmuki, P.; Mazare, A. Nanoscale Topography of Anodic TiO_2 Nanostructures Is Crucial for Cell−Surface Interactions. *ACS Appl. Mater. Interfaces* **2024**, *16* (4), 4430−4438.
(54) Fomicheva, I.; Druzhinin, P.; Amler, H.; Tesler, A. B.; Sarau, G.; Leuchs, G.; Christiansen, S. H. Formation of Laser-Induced Periodic Surface Structures on Titanium Alloy Using a Picosecond Laser: Dependence on Fluence and Number of Laser Pulses. *Adv. Mater. Interfaces* **2026**, No. e00700.
(55) Thomae, N.; Stabroth, M.; Vollmann, J.; Döring, M.; Redka, D.; Huber, H. P.; Schmidt, M. From surface roughness to crater formation in a 2D multi-scale simulation of ultrashort pulse laser ablation. *Appl. Phys. A: Mater. Sci. Process.* **2025**, *131* (1), No. 27.
(56) Wciślik, S.; Mukherjee, S. Evaluation of three methods of static contact angle measurements for TiO_2 nanofluid droplets during evaporation. *Phys. Fluid.* **2022**, *34* (6), No. 062006.

https://doi.org/10.1021/acs.langmuir.5c05888
Langmuir 2026, 42, 8269−8279